IMU/Magnetometer based 3D Indoor Positioning for wheeled Platforms in NLoS scenarios

Hendrik Hellmers, Andreas Eichhorn
Institute of Geodesy
Technische Universität Darmstadt
Darmstadt, Germany
Email: {hellmers | eichhorn}@geod.tu-darmstadt.de

Abdelmoumen Norrdine, Jörg Blankenbach
Geodetic Institute
RWTH Aachen University
Aachen, Germany
Email: {norrdine | blankenbach}@gia.rwth-aachen.de

***Abstract*—In recent years the research on localization and navigation systems in GNSS-denied environments has been focused from both industry and research. Although many technologies based on e.g. UWB, WLAN, ultrasonic or infrared have been utilized, there is still no final solution for position and orientation determination in indoor areas. The fact, that applied signals in common approaches are influenced by fading and multipath inside buildings leads to restrictions on line-of-sight (LoS) conditions.**

In contrast, the ability of penetrating any kind of building materials qualifies magnetic fields to realize object positioning in harsh indoor environments. Hence, a DC Magnetic signal based Indoor Local Positioning System (MILPS) has been developed consisting of multiple electrical coils, representing reference stations. Based on the magnetic field intensities of at least three different coils, the corresponding slope distances and therefore the observer's position can be estimated. Facing kinematic purposes a combination of MILPS and an Inertial Measurement Unit (IMU) has been applied, utilizing methods of sensor fusion.

Observed inertial data – in this case three dimensional acceleration and angular rate measurements – lead to the sensor's relative motion changes, which are processed by kinematic motion models. Based on a discrete integration with respect to the measurement time interval, the sensor's current state – consisting of position, velocity and orientation – can be predicted. These high-frequency derived predictions are furthermore supported by external MILPS-distances and elevation angles utilizing methods of Kalman Filter. Focus in this contribution lies on the processing of both inertial data and magnetic field measurements for three dimensional applications.

Keywords—3D Indoor-Positioning, DC Magnetic Fields, Quaternions, Iterative Kalman Filter

I. INTRODUCTION

Localization and navigation of moving objects are very challenging issues inside buildings, since GNSS signals are not available. However, especially with the advent of low cost multiple sensor systems – which enable observation of motion changes as well as geometrical parameters like azimuth or distances – several kinds of applications emerged which require position and orientation in indoor environments. Examples for wheeled platforms are object tracking in hospitals, positioning for robot-assistants in rescue scenarios or localization of Mobile Mapping Systems.

Because many existing approaches [1] – based on e.g. RFID [2-3], Ultra Wide Band [4-5] or ultrasound [6] – collapse due to disturbances or multipath, a Magnetic field based Indoor Local Positioning System (MILPS) was initially introduced by [7-8] and has been developed in [9-12] to focus non-line-of-sight (NLoS) scenarios. In addition to that, [13] manifests theoretical capability of IMU/MILPS integration, while [14] shows experimental results concerning simple two-dimensional motions in a building corridor.

To support applications in 3D indoor environments, this contribution aims on the signal processing of three-dimensional inertial data as well as the handling of magnetic field observations created by multiple coils.

Focusing the main goal of a moving object's three-dimensional tracking, the initial proof of concept consists of a wheeled platform's localization in a typical indoor environment. Further, the applied signal processing and utilized data models can be adopt for more complex 3D test drives. While inertial observations lead to the system's predicted state – consisting of position, velocity and orientation – the magnetic field measurements yield the corresponding slope distance and elevation angle relating to well-known reference points for update estimation using methods of Kalman filtering.

II. SYSTEM OVERVIEW

In previous contributions an IMU/Magnetometer based indoor positioning system has been presented for an object's high rated two-dimensional kinematic localization [14]. All incoming information leads to data fusion based on the method of Iterative Kalman Filter (IKF) [15], which estimates the system's current state with regard to all statistical information.

A. MILPS – Magnetic Indoor Local Positioning System

The system is based on distance and angle measurements between a mobile station and reference points by utilizing magnetic fields.

978-1-5090-2425-4/16/$31.00 ©2016 IEEE

Supplying an electric coil with a constant direct current causes a static magnetic field whose intensity decreases with the distance to its source [8]:

$$d = \sqrt[3]{\frac{\mu_0 \cdot N \cdot I \cdot F \cdot \sqrt{1 + 3 \cdot \sin^2(\varphi)}}{4\pi \cdot B}} \qquad (1)$$

Equation (1) leads to the corresponding slope distance d, where N describes the number of turns of wire, I is the current running through the coil, F expresses the base area of the coil and B is the observed magnetic field. In addition, μ_0 represents the magnetic constant and φ the elevation angle between sensor and coil.

Because the mobile station and all reference points in 2D environments are typically arranged approximately at the same height above ground, the elevation has an absolute value of zero. In three-dimensional applications, this angle has to be computed regarding all three components of the observed magnetic field by [8]

$$\varphi = \arctan\left(\frac{-3}{4}\tan(\varepsilon) \pm \sqrt{\left(\frac{3}{4}\tan(\varepsilon)\right)^2 + \frac{1}{2}}\right), \qquad (2)$$

where $\varepsilon = \arcsin\left(\frac{B_z}{\|\vec{B}\|}\right)$ describes the angle between the specific magnetic field vector $\vec{B} = (B_x\ B_y\ B_z)^T$ and the horizontal plane.

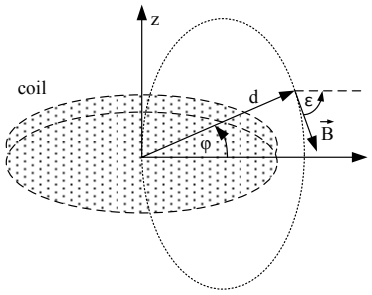

Fig. 1: Slope distance and elevation angle

However, due to interferences from other external magnetic sources, the raw observations are not usable for distance and angle determination. Beside the earth's magnetic field, electrical equipment or elevators are common disturbing sources.

To eliminate these low-frequency interferences, each coil's current direction is switched with a known switching frequency $f_s = \frac{1}{\Delta t_{coil}}$ which leads to rectangular magnetic signals, whose direction changes alternately (plus and minus subscript). Fig. 2 shows an extract of a magnetic signal captured from a sensor in rest.

Based on the differences between the arithmetic means of two subsequent clusters – which describes the constant signal while Δt_{coil} – the coil's specific magnetic field B_i can be calculated [11]:

$$B_i = \frac{B_i^+ - B_i^-}{2} \qquad (3)$$

In this case B_i^+ as well as B_i^- describe the magnetic field of coil i in positive and negative current direction respectively. In the example of Fig. 2 the magnetic field B_1 is greater than B_2 because the sensor is closer to coil 1 than to coil 2.

Although changing a coil's current direction leads to slope distance and elevation angle between user and reference point, the assumption of a rectangular signal is only valid for static magnetometers.

In motion, the clusters are distorted because the ambient magnetic field varies. The measured magnetic field is then characterized by trends which influence both subsequent clusters.

Fig. 3 shows an extract of a signal observed by a magnetometer in motion. Especially in 3D environments, where the IMU's orientation changes by driving over trafficable slopes, the captured magnetic field is affected by kinematic effects, which become apparent in trends t_A and t_B. On the assumption of a constant velocity and orientation during the switching time interval Δt_{coil}, t_A and t_B are linear. Overlay with B^+ and B^- causes biased cluster means (bold dots in Fig. 3) and thus too long or too short distances. Therefore, an average of both trends $t = \frac{t_A + t_B}{2}$ has been computed and subtracted from the raw signal, where t_A as well as t_B are – concerning each cluster – estimated as linear regressions by the method of least squares [16].

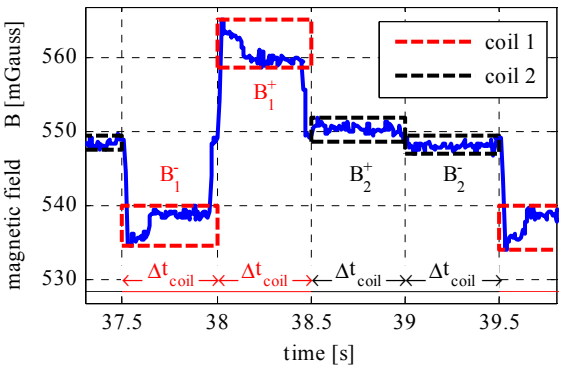

Fig. 2: Static magnetic field intensity

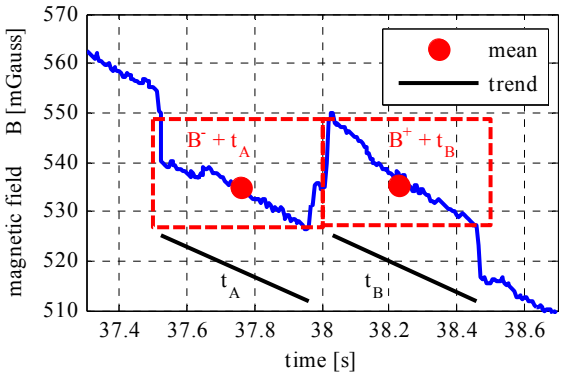

Fig. 3: Magnetic field influenced by kinematic effects

B. *Inertial Measurement Unit*

For determining high-frequency relative motion changes, the factory calibrated IMU *ADIS 16480* from *Analog Devises* has been utilized. This 10-DoF MicroElectroMechanical System (MEMS) includes a three-axial accelerometer, gyroscope and magnetometer, which ensures – beside inertial data – external distance and angle calculation between the mobile station and the reference points using MILPS.

In addition to that a barometer enables observation of air pressure.

The IMU's factory calibration delivers furthermore corrections of systematic effects on the sensor's readings. TABLE I includes some technical data [17].

TABLE I. Specification of ADIS 16480

	Acceleration [g]	**Gyroscope [°/s]**	**Magnetometer [mGauss]**
Dynamic Range	-10 to 10	-450 to 450	-2.5 to 2.5
Resolution	$1.221 \cdot 10^{-8}$	$3.05 \cdot 10^{-7}$	$1 \cdot 10^{-4}$
Output Noise	0.0015	0.16	0.45

In order to eliminate remaining parts of gyroscope or acceleration offsets, an initial data acquisition has been performed based on a stationary IMU before each test drive. The corresponding average values – in the area of 10^{-2} °/s respectively $\mathrm{m/s^2}$ – were assumed as constant remaining drifts and have been eliminated from all initial signals.

Furthermore, to describe the platform's movement with respect to the IMU's body frame – characterized by the sensor axes – different steps of signal processing have been applied, for eliminating high frequency noise and outliers (chapter III).

Finally, extracted acceleration and angular rate measurements have to be transferred from the body frame to a local coordinate system – defined e.g. by building axes – which is realized by the motion model in chapter IV.

III. Signal Processing

Calculating a vehicle's kinematic state using acceleration and gyroscope measurements, high frequency interferences – caused by platform vibrations and bumps during test drive – have to be eliminated.

Thereby, a low pass filter removes noise components in a first step, while real accelerations and angular rates are extracted utilizing a peak detection based on predefined thresholds.

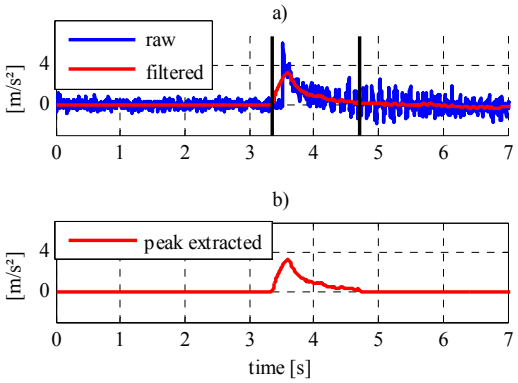

Fig. 4: Captured acceleration (x-direction)

The blue graph in Fig. 4a shows an extract of the captured acceleration signal in the direction of the platform's movement. In order to eliminate evident high frequency noise – especially while driving – a moving average over the whole signal has been applied [18]. Thereby, the specific average order results from the acceleration peaks' amplitude spectrum.

Regarding the received noise-attenuated acceleration signal (red graph) makes clear, that an actual velocity change in this example appears during the time interval $t = 3.4$ s to $t = 4.6$ s (illustrated by vertical lines). Over this period, the signal rises above a predefined threshold and will be hence extracted. Setting remaining signal values to zero leads to the significant acceleration in Fig. 4b. Thus, impacts of a rough drive caused by the ground's bumpiness are consequently eliminated.

In addition to this, Fig. 5 shows an extract of a captured angular rate signal, from which the platform's orientation can be estimated.

The described signal processing and peak detection leads to acceleration signals with an absolute value of zero at constant velocities. For this reason, orientation changing has to be determined utilizing the present velocity and relative orientation changes – represented by gyroscope readings – with respect to the current orientation. Therefore, constraints about sequential rotations and transition to quaternion representation for the motion model have to be considered in section IV.

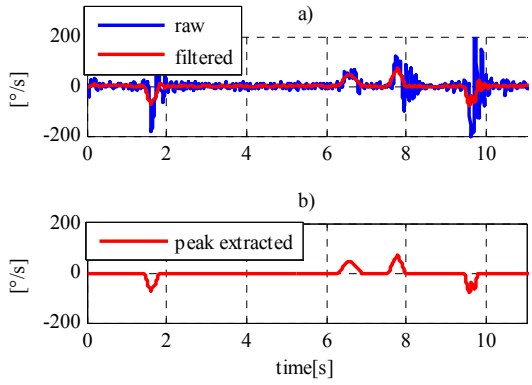

Fig. 5: Captured angular rates (y-direction)

IV. State Estimation

To describe an object's three-dimensional kinematic state with respect to a local coordinate system based on inertial data, the body frame's orientation must be calculated relative to this local frame at every discrete time step k. Therefore, principle of sequential rotations is introduced in subsection A, while subsection B explains functionalities of quaternion algebra. Finally, subsection C describes the applied motion model.

A. Sequential Rotations

Angular rates update a sensor's orientation in a local frame applying a discrete integration with respect to measurement time interval Δt. Because the observed inertial data refers to the sensor's axes at timestamp k, the derived orientation changes from k to k+1 can be considered as rotations with reference to the body frame's current axes.

In the following, the rotation matrix $R_k \in \mathbb{R}^{3\times3}$ – which describes orientation at timestamp k – rotates the body frame into the local frame. The orientation changing from k to k+1 is expressed by $\Delta R_{k+1} \in \mathbb{R}^{3\times3}$. Vectors are illustrated with bolt lower cases, while matrices are represented with upper cases. Scalars are expressed as thin lower cases.

The sensor's orientation at timestamp k is given by rotating the initial direction of travel $\mathbf{v}_0 \in \mathbb{R}^{3\times1}$ with R_k [19]:

$$\mathbf{v}_k = R_k \cdot \mathbf{v}_0 \tag{4}$$

The axes of the body frame and the local frame are congruent at k=0.

For describing an orientation changing of $\mathbf{v}_k$ with respect to the follower axes – characterized by R_k – this rotation has to be reversed using R_k^{-1}. The regained initial orientation is then rotated at first by ΔR_{k+1} and finally rotated by R_k, which realises an orientation changing from timestamp k to k+1 relative to the sensor's current axes [19]:

$$\mathbf{v}_{k+1} = R_k \cdot \Delta R_{k+1} \cdot R_k^{-1} \cdot R_k \cdot \mathbf{v}_0 \tag{5}$$

With $R_k^{-1} \cdot R_k = \mathbb{I}$ and $R_k^{-1} = R_k^T$ follows:

$$\mathbf{v}_{k+1} = R_k \cdot \Delta R_{k+1} \cdot \mathbf{v}_0 \tag{6}$$

and

$$\mathbf{v}_{k+1} = R_k \cdot \Delta R_{k+1} \cdot R_k^T \cdot \mathbf{v}_k \tag{7}$$

B. Quaternions

Quaternions are mathematical notations for describing three dimensional rotations. Unlike Euler angles, they avoid singularities and the problem of gimbal lock. A quaternion $\mathbf{q}$ is thereby defined as a four dimensional vector [20]:

$$\mathbf{q} = (q_0\ q_1\ q_2\ q_3), \tag{8}$$

where q_0 is the scalar part and q_1, q_2 and q_3 describe the vector part. A right- and left-sided multiplication of a quaternion $\mathbf{p}$ with $\mathbf{q}$ and its inverse $\mathbf{q}^{-1}$ rotates the vector part of $\mathbf{p}$ to $\mathbf{p}'$ [18]:

$$\mathbf{p}' = \mathbf{q} \cdot \mathbf{p} \cdot \mathbf{q}^{-1}, \tag{9}$$

where $\mathbf{q} \cdot \mathbf{q}^{-1} = (1\ 0\ 0\ 0)$. A quaternion multiplication $\mathbf{q} \cdot \mathbf{p}$ is thereby defined as [20]:

$$\mathbf{q} \cdot \mathbf{p} = \begin{pmatrix} q_0p_0 - q_1p_1 - q_2p_2 - q_3p_3 \\ q_1p_0 + q_0p_1 - q_3p_2 + q_2p_3 \\ q_2p_0 + q_3p_1 + q_0p_2 - q_1p_3 \\ q_3p_0 - q_2p_1 + q_1p_2 + q_0p_3 \end{pmatrix} \tag{10}$$

Furthermore, two consecutive rotations of $\mathbf{p}$ with a rotation I (quaternion $\mathbf{r}$) and a rotation II (quaternion $\mathbf{q}$) lead to the quaternion multiplication [20]

$$\mathbf{p}' = \mathbf{qr} \cdot \mathbf{p} \cdot (\mathbf{qr})^{-1}, \tag{11}$$

where rotation II refers to axes accordingly rotated by I, which is equivalent to (6). Finally, regarding (10) this sequential rotation can be expressed as the matrix-vector product:

$$\mathbf{q} \cdot \mathbf{r} = \begin{pmatrix} r_0 & -r_1 & -r_2 & -r_3 \\ r_1 & r_0 & r_3 & -r_2 \\ r_2 & -r_3 & r_0 & r_1 \\ r_3 & r_2 & -r_1 & r_0 \end{pmatrix} \cdot \begin{pmatrix} q_0 \\ q_1 \\ q_2 \\ q_3 \end{pmatrix} \tag{12}$$

The Calculation of the corresponding rotation matrix R as a function of $\mathbf{q}$ is shown in [21].

C. Dead Reckonig

To illustrate an object's kinematic state, the method of *dead reckoning* is applied, which yields position, velocity and orientation by utilizing discrete integrations with respect to Δt regarding acceleration measurements $\mathbf{u}_{k+1} = (\ddot{x}\ \ddot{y}\ \ddot{z})^T$ and angular rates $\boldsymbol{\psi}_{k+1} = (\omega_x\ \omega_y\ \omega_z)^T$. The system's current state vector

$$\mathbf{x} = (x\ y\ z\ \dot{x}\ \dot{y}\ \dot{z}\ q_0\ q_1\ q_2\ q_3)^T \tag{13}$$

is thereby determined at every discrete timestamp k, where $(x\ y\ z)^T$ describe the position, $(\dot{x}\ \dot{y}\ \dot{z})^T$ the velocity and $(q_0\ q_1\ q_2\ q_3)^T$ the orientation. Based on $\mathbf{u}$ and $\boldsymbol{\psi}$, the current state at timestamp k+1 can be predicted by applying *equation of motion* [14]

$$\mathbf{x}_{k+1} = \Phi \cdot \mathbf{x}_k + C \cdot R(\mathbf{q}_{k+1}) \cdot \mathbf{u}_{k+1}, \tag{14}$$

where Φ stands for the transition matrix, C for the control matrix and $\mathbf{u}$ for the acceleration vector. R describes the rotation between body frame and local frame. Thereby the transition matrix Φ consists of four sub matrices realising the transfer from state at time step k to k+1:

$$\Phi = \begin{pmatrix} \Phi_{1,1} & 0^{6\times4} \\ 0^{4\times6} & \Phi_{2,2} \end{pmatrix} \tag{15}$$

To transform the velocity (entries 4-6 of $\mathbf{x}$) from timestamp k to k+1, a rotation with observed angular rates $\boldsymbol{\psi}_{k+1}$ relating to the current orientation $\mathbf{q}_k$ has to be applied. Because high

sample rates lead to small angular rate measurements, the orientation changing matrix can be expressed as [21]

$$\Delta R = \begin{pmatrix} 1 & -\omega_z \cdot \Delta t & \omega_y \cdot \Delta t \\ \omega_z \cdot \Delta t & 1 & -\omega_x \cdot \Delta t \\ -\omega_y \cdot \Delta t & \omega_x \cdot \Delta t & 1 \end{pmatrix} \tag{16}$$

by using the approximations:

$$\sin(\omega \cdot \Delta t) \approx \omega \cdot \Delta t \text{ and } \cos(\omega \cdot \Delta t) \approx 1. \tag{17}$$

From (7), the update of the velocity's direction is given by

$$V = R_k \cdot \Delta R_{k+1} \cdot R_k^T \tag{18}$$

which leads to the sub matrix:

$$\Phi_{1,1} = \begin{pmatrix} 1 & 0 & 0 & \Delta t & 0 & 0 \\ 0 & 1 & 0 & 0 & \Delta t & 0 \\ 0 & 0 & 1 & 0 & 0 & \Delta t \\ 0 & 0 & 0 & V_{1,1} & V_{1,2} & V_{1,3} \\ 0 & 0 & 0 & V_{2,1} & V_{2,2} & V_{2,3} \\ 0 & 0 & 0 & V_{3,1} & V_{3,2} & V_{3,3} \end{pmatrix} \tag{19}$$

Furthermore, the corresponding quaternion $\Delta\mathbf{q}$ of small angular rates can be expressed as [21]:

$$\Delta\mathbf{q} = \begin{pmatrix} 1 \\ \Delta t \cdot \omega_x/2 \\ \Delta t \cdot \omega_y/2 \\ \Delta t \cdot \omega_z/2 \end{pmatrix} \tag{20}$$

Inserting (20) in equation (12) yields the orientation's update matrix, which transfers $\mathbf{q}_k$ to $\mathbf{q}_{k+1}$:

$$\Phi_{2,2} = \frac{\Delta t}{2} \cdot \begin{pmatrix} 2/\Delta t & -\omega_x & -\omega_y & -\omega_z \\ \omega_x & 2/\Delta t & \omega_z & -\omega_y \\ \omega_y & -\omega_z & 2/\Delta t & \omega_x \\ \omega_z & \omega_y & -\omega_x & 2/\Delta t \end{pmatrix} \tag{21}$$

Finally, the control matrix C realizes integration of acceleration measurements with respect to Δt [14]:

$$C = \begin{pmatrix} \Delta t^2/2 & 0 & 0 \\ 0 & \Delta t^2/2 & 0 \\ 0 & 0 & \Delta t^2/2 \\ \Delta t & 0 & 0 \\ 0 & \Delta t & 0 \\ 0 & 0 & \Delta t \\ 0 & 0 & 0 \\ 0 & 0 & 0 \\ 0 & 0 & 0 \\ 0 & 0 & 0 \end{pmatrix} \tag{22}$$

A brief introduction in the method of Iterated Kalman Filter as update process when MILPS-measurements are available is given in the next chapter. Therefore, the variance propagation from timestamp k to k+1 for weightings in IKF process can then be determined by [21]

$$(Q_{xx}^-)_{k+1} = \Phi \cdot (Q_{xx}^-)_k \cdot \Phi^T + (C \cdot R_k) \cdot Q_{uu} \cdot (C \cdot R_k)^T, \tag{23}$$

where Q_{xx} and Q_{uu} represent the state's and the acceleration vector's cofactor matrix respectively.

D. Iterative Kalman Filter

For updating the state's prediction $\mathbf{x}^-$and its predicted cofactor matrix Q_{xx}^- in Kalman Filter process, the method of IKF has been applied if MILPS-data are available [14].

Thereby, the observation model $\mathbf{f} = (\mathbf{r}, \boldsymbol{\theta})$ includes both the slope distances $\mathbf{r} = (r_1, \dots, r_m)$ as well as the elevation angles $\boldsymbol{\theta} = (\theta_1, \dots, \theta_m)$ between the current position and the reference point's coordinates $(x_i^{RP}, y_i^{RP}, z_i^{RP}), \{i = 1, \dots, m\}$:

$$r_i = \sqrt{(x_i^{RP} - x)^2 + (y_i^{RP} - y)^2 + (z_i^{RP} - z)^2} \tag{24}$$

$$\theta_i = \arcsin\left(\frac{z - z_i^{RP}}{r_i}\right) \tag{25}$$

In this context m is the total number of accessible coils. The *Jacobian* H_j after j iterations is given with respect to $\mathbf{x}$

$$H_j = \frac{\partial \mathbf{f}(\mathbf{x})}{\partial \mathbf{x}}\Big|_{\mathbf{x}=\mathbf{x}_j} \text{ with } \mathbf{x}_0 = \mathbf{x}^-, \tag{26}$$

which leads to the *Kalman Matrix* K_j for the observations' weighting [15]:

$$K_j = Q_{xx}^- \cdot H_j^T \cdot (H_j \cdot Q_{xx}^- \cdot H_j^T + Q_{ll})^{-1} \tag{27}$$

Thereby Q_{ll} represents the cofactor matrix of the distance and elevation measurements illustrated in (1) and (2):

$$\mathbf{l} = (d_1, \dots, d_m, \varphi_1, \dots, \varphi_m) \tag{28}$$

Finally, the new state estimate of the j^{th} iteration can be estimated [15]:

$$\mathbf{x}_{j+1} = \mathbf{x}^- + K_j \cdot (\mathbf{l} - \mathbf{f}(\mathbf{x}_j) - H_j \cdot (\mathbf{x}^- - \mathbf{x}_j)) \tag{29}$$

Until convergence is reached, steps (26) – (28) are executed iteratively, so that the state update $\mathbf{x}^+ = \mathbf{x}_{j+1}$ and its cofactor matrix

$$Q_{xx}^+ = (\mathbb{I} - K_j \cdot H_j) \cdot Q_{xx}^- \tag{30}$$

can be determined.

V. POSITIONING

To test the described IMU/MILPS sensor fusion for precise localization of wheeled platforms in NLoS scenarios, a measurement ride based on a remotely controlled vehicle is organized. Driven by a DC electric motor, the platform is able to reach a velocity of up to 5 m/s. Furthermore, the platform has a dimension of about 0.4 × 0.3 m and is equipped with the MEMS IMU and a mainboard for data logging (Fig. 6).

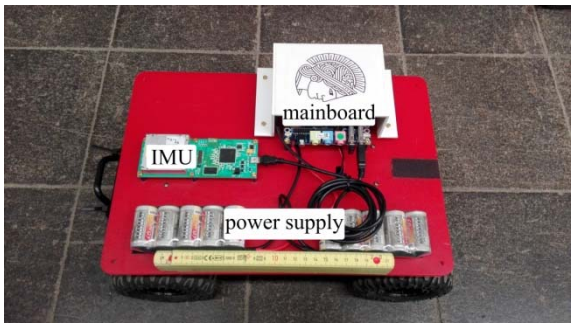

Fig. 6: Remote-controlled platform

For proofing the concept, a measurement ride on a building floor with a simple wheeled cart has been performed. This tracking experiment was realized inside a NLoS indoor environment characterized by a test trajectory consisting of six track points whose coordinates are defined by a local frame. Furthermore, three coils as reference stations have been placed on known coordinates for realizing distance and elevation measurements.

All fixed points' positions – reference points as well as track points – were determined using a tacheometer, leading to a point precision of better than 1 cm and have been marked on the ground floor covered by an area of about 200 m² of RWTH Aachen University. Although this system is suitable for real time positioning, in this case data post-processing has been applied for testing the described algorithms. Fig. 7 shows a true-to-scale drawing of that test area.

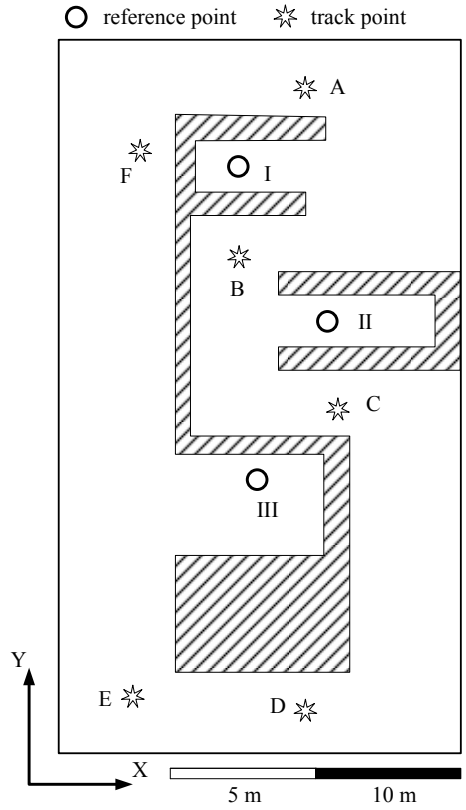

Fig. 7: Positioning test area

Dashed parts represent inaccessible areas in this NLoS scenario. Driving through different rooms and the floor's central corridor leads to a usual occurrence of direction-, and velocity changes.

The IMU has been installed horizontally and inertial data acquisition as well as magnetic field observation has been carried out applying a sample rate of $\frac{1}{\Delta t} = 200$ Hz.

Starting on position A, the vehicle has been moved four times over the whole track ($A \rightarrow B \rightarrow C \rightarrow D \rightarrow E \rightarrow F$) and was finally stopped at the starting point again. While passing the known track points absolute timestamps have been captured for performing a comparison to the true position values (chapter VI).

For providing MILPS-data, the coils' current supply was switched consecutively based on a switching time interval of $\Delta t_{coil} = 0.3$ s to reach nearly quasi-static signals for magnetic signal processing. Cluster separation (Fig. 3) is then realized by regarding absolute switching intervals.

In order to reconstruct the trajectory based on integrated inertial data, the initial system state $\mathbf{x}_0$ – consisting of the starting point's coordinates, the velocity of zero and the initial heading – was predefined. Furthermore, the initial state's cofactor matrix $(Q_{xx})_0$ as well as a constant control vector's cofactor matrix $Q_{uu} = diag(\sigma_u)$ has been set up. Thereby σ_u represents the IMU's output noise (TABLE I).

In addition to that, the external distance and elevation measurements' precisions were adopted proportionally to the corresponding distance's square root in the applied Kalman Filter process. This is due to the measurements' precisions decrease with the absolute distance to the specific coil.

VI. Results

To evaluate the sensor fusion performance, the platform was moved along the trajectory (Fig. 7) with an average speed of about 1.2 m/s. Switching the coils' current direction with a switching interval of Δt_{coil} provides – depending on the coils reachability – external distances and elevation angle measurements every 1-2 seconds by applying (1) and (2).

Fig. 8 shows tracking results of the test drive with respect to the horizontal x/y-plane. Because the coils as well as the mobile platform were placed approximately in the same high, calculated z-values are only diagrammed in a true-calculated comparison.

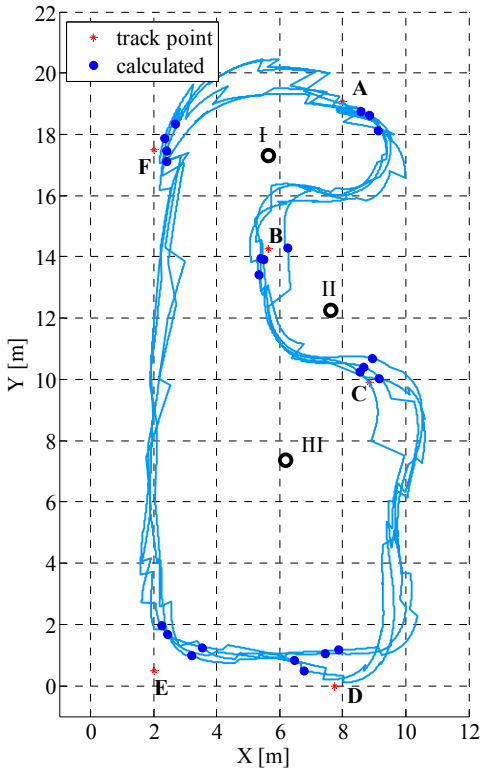

Fig. 8: Tracking results (x/y plane)

The computed positions of all track points – identified by taking time stamps when passing the markings on the floor – are illustrated with bold dots. It becomes evident, that a stable solution can be reached during the whole measured drive with an accuracy of 0.5 – 1.5 m. In contrast to the IMU's inertial data, external MILPS-distances and elevation angles are not dependent from previous solutions which makes them long-term stable and therefore feasible for data support in Kalman Filter process. The comparison of true and calculated coordinates at all passed tracking points confirms this assumption.

Fig. 9 shows the horizontal deviations between computed and true track points. A maximal deviation of about 1.5 m lead to the conclusion – in a first step – that reliable localization concerning moving platforms in indoor environments can be reached.

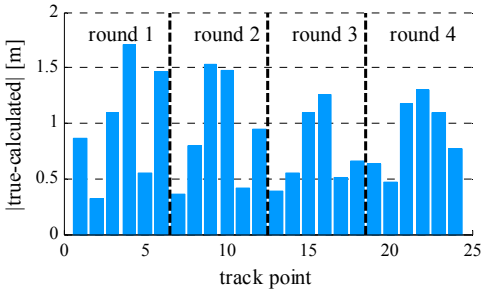

Fig. 9: Comparison at track points (x/y plane)

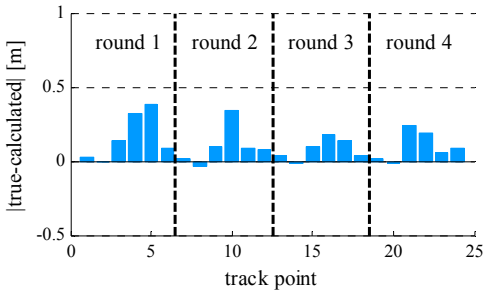

Fig. 10: Comparison at track points (z-value)

In addition to that, Fig. 10 shows the corresponding comparison of the calculated height. Although the test drive was based on a horizontal track, the vehicle's z-coordinate changes because of the applied elevation angle in Kalman Filter process. Thereby, a maximal deviation of below 0.5 m confirms the assumption of reaching reliable positioning results of 3D indoor localization using sensor fusion based on inertial data and magnetic fields.

VII. Conclusion and Outlook

This contribution aims on signal processing for an IMU/Magnetometer based indoor localization system. Captured inertial data as well as observed external geometrical parameters have been processed based on methods of Kalman Filter. Thereby, overlays caused by kinematic effects have been eliminated for reaching reliable distance and elevation measurements between mobile station and reference points. Applying suitable assumptions of all observations' statistic leads to a best estimation of a system's current state.

Although the calculations in this work are based on data post-processing utilizing MATLAB, both applied signal processing and algorithm of Kalman Filter are little computationally intensive and consequently real-time capable.

The results show, that positioning can be reached with an accuracy of 0.5-1.5 m with respect to the horizontal plane as well as to the z-value in a typical indoor environment. Further investigations, accordingly, will focus on reliable real-time positioning for wheeled platforms in complex 3D NLoS environments consisting of significant altitude changes.

References

[1] Mautz, Rainer: Indoor Positioning Technoligies, Habilitation Thesis submitted to ETH Zurich, Institute of Geodesy and Photogrammetry, Department of Civil, Environmental and Geomatic Engineering, ETH Zurich, Februar 2012

[2] Han Zou ; Hengtao Wang ; Lihua Xie ; Qing-Shan Jia, An RFID Indoor Positioning System by Using Weighted Path Loss and Extreme Learning Machine, 2013 IEEE 1st International Conference on Cyber-Physical Systems, Networks, and Applications (CPSNA)

[3] A. Ruiz, F. Granja, J. Honorato, and J. Rosas, “Pedestrian indoor navigation by aiding a foot-mounted imu with rfid signal strength mesurements”, 2010 International Conference on Indoor Positioning and Indoor Navigation (IPIN), 2010, pp. 1–7

[4] C. Ascher, L. Zwirello, T. Zwick and O.Trommer, "Integrity monitoring for UWB/INS tightly coupled pedestrian indoor scenarios", 2011 International Conference on Indoor Positioning and Indoor Navigation (lPIN), 2011, pp.1-6

[5] P. Meissner, T. Gigl, and K. Witrisal, “UWB sequential Monte Carlo positioning using virtual anchors”, 2010 International Conference on Indoor Positioning and IndoorNavigation (IPIN), 2010, pp. 1–10

[6] S. Holm, "Ultrasound positioning based on time-of- flight and signal strength", 2012 International Conference on Indoor Positioning and Indoor Navigation (IPIN) pp. 1-6

[7] A. Norrdine, Präzise Positionierung und Orientierung innerhalb von Gebäuden, Dissertation, Schriftenreihe der Fachrichtung Geodäsie, Fachbereich Bauingenieurwesen und Geodäsie, Technische Universität Darmstadt, Mai 2009

[8] E. Prigge: A Positioning System with No Line-of-sight Restrictions for Cluttered Environments. Stanford University.

[9] Blankenbach J. und Norrdine, A., Position Estimation Using Artificial Generated Magnetic Fields, IEEE Xplore Proceedings of 2010 International Conference on Indoor Positioning and Indoor Navigation, 15-17 September 2010, Zürich, Switzerland

[10] J. Blankenbach, A. Norrdine (2015): Magnetic Indoor Local Positioning System. Book chapter, In: Kamini (eds.): Indoor Wayfinding and Navigation, CRC Press, Boca Raton, ISBN 978-1-4822-3085-7, pp. 53-80

[11] Blankenbach, J., Norrdine, A. und Hellmers, H., A robust and precise 3D indoor positioning system for harsh environments, IEEE Xplore Proceedings of the 2012 International Conference on Indoor Positioning and Indoor Navigation, 13-15 November 2012, Sydney, Australia

[12] Kasmi, Z.; Norrdine, A.; Blankenbach, J.: Towards a Decentralized Magnetic Indoor Positioning System. Sensors 2015, 15, 30319-30339

[13] H. Hellmers, A. Norrdine, J. Blankenbach, A. Eichhorn: An IMU/Magnetometer-based Indoor Positioning System using Kalman Filtering. Proc. of 2013 International Conference on Indoor Positioning and Indoor Navigation (IPIN), 28-31 October 2013, Montbéliard, France

[14] H. Hellmers, A. Norrdine, J. Blankenbach, A. Eichhorn: Indoor Localisation for wheeled Platforms based on IMU and artificially generated Magnetic Field. Proc. of 2014 Ubiquitous Positioning Indoor Navigation and Location Based Service (UPINLBS), 20- 21 November 2014, Corpus Christi, Texas, USA

[15] G. Welch and G. Bishop, “An introduction to the Kalman filter,” University of North Carolina at Chapel Hill, ChapelHill, NC, 1995.

[16] Wolfgang Niemeier, Ausgleichungsrechnung, De Gruyter Lehrbuch, Berlin 2001

[17] Analog Devices, Ten Degrees of Freedom Inertial Sensor with Dynamic Orientation Outputs (ADIS 16480), Data Sheet

[18] Kreiß,J. Neuhaus,G., Einführung in die Zeitreihenanalyse, Springer Verlag, Berlin Heidelber 2006

[19] Rebecca M. Brannon, ROTATION: A review of useful theorems involving proper orthogonal matrices referenced to three dimensional physical space, Computational Physics and Mechanics, Sandia National Laboratories, Albuquerque, NM

[20] Jack B. Kuipers, Quaternions and Rotation Sequences, Department of Mathematics, Calvin College, Grand Rapids, MI 49546, USA

[21] J. Wendel, Integrierte Navigationssysteme (Sensorfusion, GPS und Inertiale Navigation), 2. Auflage, Oldenbourg Verlag, München 2011